JM PAPERS

Libration-driven topographic Rossby waves in a tilted cube

Ke Wu[1] , Bruno D. Welfert[2] and Juan M. Lopez[2]

[1]School of Mathematical Science, University of Electronic Science and Technology of China, Sichuan 611731, PR China

[2]School of Mathematical and Statistical Sciences, Arizona State University, Tempe, AZ 85287, USA

Corresponding author: Juan M. Lopez, juan.m.lopez@asu.edu

The flow of an incompressible fluid in a rapidly rotating cubic cavity librating at a low frequency around an axis through the midpoints of opposite edges features synchronous waves with a foliation pattern that is quasi-invariant in the axial direction. These waves are emitted from the equatorial edges (the edges furthest away from the axis) and travel into the interior in a retrograde fashion about the eastern equatorial vertices. These waves are interpreted as topographic Rossby waves, consistent with the lack of closed geostrophic contours for the rotating container. They are analysed in detail at small Ekman numbers, both in the linear regime, corresponding to the limit of zero libration amplitude (Rossby number $Ro \to 0$), and in the weakly nonlinear regime with small but finite Ro. The waves subsist in the linear regime and coexist with a network of shear layers that are predicted by linear inviscid analysis to focus towards the equatorial edges. However, viscous effects stop the focusing at a distance from the edges that scales with $E^{1/2}$. The large inclination of the oblique walls with the rotation axis, together with the vanishing depth at the equatorial edges, provide the conditions for singular behaviour in the Rossby waves as $E \to 0$. Within a distance of the eastern equatorial vertices also scaling with $E^{1/2}$, the nonlinear contributions have a self-similar structure whose enstrophy density scales as $E^{-16/3} Ro^2$. This means that Ro must be reduced considerably faster than E for nonlinear contributions to be negligible as $E \to 0$.

Key words: rotating flows

1. Introduction

Rapidly rotating contained flows subjected to small-amplitude temporal modulations can result in a myriad of intriguing response flows, even in containers with very

simple geometry. How rapidly the container is rotating is quantified by the Ekman number E, which is the ratio of the rotation period and the viscous time scale, and the magnitude of the temporal modulation force is quantified by a Rossby number Ro. In physical settings, these non-dimensional numbers are small but non-zero. The types of response flows include inertial container modes (Lord Kelvin 1880; Greenspan 1968) as well as thin internal shear layers consisting of circularly polarised wavebeams (Wood 1966) with peculiar reflection properties. When the wall normal is oblique to the rotation axis, the reflections of these wavebeams generally result in geometric focusing, whereby their wavelength decreases and their energy increases (Phillips 1963). Furthermore, their eventual trajectories tend to converge to so-called attractors, located either at edges or vertices of the container (Greenspan 1969) or in the interior of the container (Rieutord *et al.* 2000, 2001; Maas 2001; Manders & Maas 2003; Boury *et al.* 2021; Subbotin *et al.* 2023; Welfert, Lopez & Wu 2023; Wu, Welfert & Lopez 2023; Shiryaeva, Subbotina & Subbotin 2024).

Response flows driven by libration in a cube rapidly rotating around an axis passing through the midpoints of two diagonally opposite edges have been shown to possess a novel feature for low libration frequencies, consisting of foliated retrograde progressive waves. These are synchronous with the librational forcing and are quasi-invariant in the direction of the rotation axis (Wu *et al.* 2022*b*). At very small libration frequencies, shear layers are also emitted from various edges and vertices and undergo many reflections on the oblique walls as they focus towards attractors at the equatorial edges, the edges furthest away from the rotation axis adjoining the oblique walls. In a linear inviscid idealisation, these edge attractors act as black holes where, as noted by Greenspan (1969), no linear inviscid mechanism exists which allows the wavebeams that focus onto the attractor to return to the interior except total reflection from an intense singularity at the attractor. At the focusing reflections, the enstrophy density in the shear layers is enhanced not only via geometric focusing (Phillips 1963), but also via vortex tilting and stretching taking place in the very localised region of the reflections for small but non-zero Ro (Wu *et al.* 2022*b*). While viscosity regularises the thickness of the shear layers for small but non-zero E, we also find that viscosity completely arrests the focusing of the beams before they reach their inviscid focusing limits at the edges. This allows for the foliated retrograde progressive waves to be observed unimpeded in these regions.

In this study, we revisit the foliated progressive waves at a low libration frequency and report new insights. This orientation of the rotating cube lacks closed geostrophic contours, for which linear inviscid theory predicts the presence of topographic Rossby waves (Pedlosky & Greenspan 1967; Beardsley 1975). We explore how such waves and the foliations are related by substantially increasing the spatial and temporal resolutions to obtain numerical results down to $E = 10^{-9}$. Furthermore, for these small-E flows, we also consider the zero-Rossby-number limit and show that these foliations persist in the linear response flows. Then, by decomposing the small-Rossby-number flows into the linear zero-Rossby-number flow and the nonlinear oscillations, we find that the nonlinear oscillations are very localised near the eastern equatorial vertices of the cube about which the foliation patterns quasi-rotate. This is used to provide guidance on how small Ro needs to be in order for nonlinear effects to be negligible. This upper limit on Ro decreases rapidly with decreasing E due to the development of extremely large gradients localised near these eastern equatorial vertices.

The results presented here provide new insights into the role of nonlinearities in flows that have traditionally been studied from a linearised inviscid perspective. Recent theoretical studies providing viscous and nonlinear corrections have been restricted to idealised settings, such as in Le Dizès (2020) who studied circularly polarised wavebeams
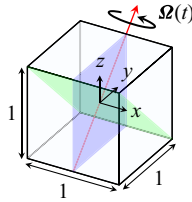
Figure 1. Schematic of the cube librating around the rotation axis $\boldsymbol{\Omega}(t)$, with the meridional plane $x = 0$ shown in blue and the equatorial plane $y = -z$ shown in green.

reflecting on a wall in semi-unbounded space, finding that, while the second-harmonic correction is purely inviscid, the mean-flow correction is of a different nature involving complicated viscous processes along with nonlinear processes. In Le Dizès (2024), a similar analysis was used for circularly polarised wavebeams at a critical slope singularity, again in semi-unbounded space, and noted that extending the analysis technique to a fully enclosed domain is a complicated issue. Those studies considered interactions between incident and reflected circularly polarised wavebeams, but being semi-unbounded, did not contemplate issues associated with coexisting cavity modes, which are generally not circularly polarised waves. The fully enclosed cavity modes include the foliation patterned topographic Rossby waves that we explore here.

2. Governing equations

A cube of side length L is completely filled with an incompressible fluid of kinematic viscosity ν. It rotates around an axis passing through the midpoints of opposite edges at a mean rate Ω that is modulated harmonically at a frequency σ with amplitude δ. The system is non-dimensionalised using L as the length scale and $1/\Omega$ as the time scale, and is described in terms of a non-dimensional Cartesian coordinate system $\boldsymbol{x} = (x, y, z) \in [-0.5, 0.5]^3$ that is fixed in the cube, with the origin at the centre. The non-dimensional angular velocity is

$$\boldsymbol{\Omega}(t) = [1 + Ro\cos(2\omega t)]\boldsymbol{\Omega}_0 , \quad \boldsymbol{\Omega}_0 = (0, 1, 1)/\sqrt{2}, \tag{2.1}$$

where the non-dimensional libration frequency is

$$2\omega = \sigma/\Omega \tag{2.2}$$

and the relative amplitude is the Rossby number

$$Ro = \delta/\Omega. \tag{2.3}$$

Figure 1 shows a schematic of the system. The two walls at $x = \pm 0.5$ are parallel to the rotation axis $\boldsymbol{\Omega}_0$ and the four remaining walls are inclined at angles $\pm 45°$ relative to $\boldsymbol{\Omega}_0$. Four of the edges are orthogonal to $\boldsymbol{\Omega}_0$. The two bisected by the rotation axis are termed the north and south polar edges and the vertices at their ends are polar vertices. The other two edges are the equatorial edges with equatorial vertices at their ends. The two vertices at $(x, y, z) = (\pm 0.5, \mp 0.5, \pm 0.5)$ are the eastern equatorial vertices and the two vertices at $(\mp 0.5, \mp 0.5, \pm 0.5)$ are the western equatorial vertices. The remaining eight edges are inclined at angles $\pm 45°$ relative to $\boldsymbol{\Omega}_0$; these are tropical edges, each with a polar and an equatorial vertex at their ends. The depth is the distance parallel to the rotation axis between the top and bottom inclined walls; this varies from $\sqrt{2}$ between the polar edges to 0 at the equatorial edges. Also shown in the schematic are the meridional plane $x = 0$ in blue and the equatorial plane $y = -z$ in green.

In the frame of reference fixed to the cube, the non-dimensional Navier–Stokes equations for the relative velocity $\boldsymbol{u}$ are

$$\frac{\partial \boldsymbol{u}}{\partial t} + (\boldsymbol{u} \cdot \nabla)\boldsymbol{u} + \nabla p - E\nabla^2 \boldsymbol{u} + 2\boldsymbol{\Omega} \times \boldsymbol{u} = -\frac{\mathrm{d}\boldsymbol{\Omega}}{\mathrm{d}t} \times \boldsymbol{x}, \quad \nabla \cdot \boldsymbol{u} = 0, \qquad (2.4)$$

where p is the reduced pressure incorporating the centrifugal force and

$$E = \nu/(\Omega\,L^2) \qquad (2.5)$$

is the Ekman number. The last term on the left-hand side of (2.4) is the Coriolis force that includes a time-harmonic component from the librational forcing. The right-hand-side term is the time-harmonic Euler force also corresponding to the librational forcing. The boundary conditions are no-slip, $\boldsymbol{u} = \boldsymbol{0}$, on all walls of the cube.

In the small-forcing regime, $0 < Ro \ll 1$, the magnitude of the response flow is of the order of Ro, and it is convenient to rescale the velocity and pressure by introducing

$$\boldsymbol{v} = \boldsymbol{u}/Ro \quad \text{and} \quad q = p/Ro, \qquad (2.6)$$

with corresponding vorticity $\nabla \times \boldsymbol{v}$ and enstrophy density $(\nabla \times \boldsymbol{v})^2$. The system (2.4) then becomes

$$\frac{\partial \boldsymbol{v}}{\partial t} + Ro(\boldsymbol{v} \cdot \nabla)\boldsymbol{v} + \nabla q - E\nabla^2 \boldsymbol{v} + 2[1 + Ro\cos(2\omega t)]\boldsymbol{\Omega}_0 \times \boldsymbol{v} = \boldsymbol{f}, \quad \nabla \cdot \boldsymbol{v} = 0,$$
$$(2.7)$$

where the scaled Euler force is

$$\boldsymbol{f} = 2\omega \sin(2\omega t)\,\boldsymbol{\Omega}_0 \times \boldsymbol{x}. \qquad (2.8)$$

The systems (2.4) and (2.7) are only equivalent for $Ro \neq 0$. Indeed, for $Ro = 0$ (2.4) remains nonlinear, but unforced, with trivial solution $(\boldsymbol{u}, p) = (\boldsymbol{0}, 0)$, while (2.7) reduces to the linear forced system

$$\frac{\partial \boldsymbol{v}_0}{\partial t} + \nabla q_0 - E\nabla^2 \boldsymbol{v}_0 + 2\boldsymbol{\Omega}_0 \times \boldsymbol{v}_0 = \boldsymbol{f}, \quad \nabla \cdot \boldsymbol{v}_0 = 0, \qquad (2.9)$$

with non-trivial solutions $(\boldsymbol{v}_0, q_0) = (\boldsymbol{v}, q)|_{Ro=0}$. The system (2.9) provides a convenient way to explore the small-Ro limit in an asymptotic sense, namely $(\boldsymbol{u}, p) \approx Ro(\boldsymbol{v}_0, q_0)$ for sufficiently small Ro.

3. Numerics

The numerical scheme for solving the governing equations (2.7) is based on a consistent splitting scheme for the Navier–Stokes equations with no-slip boundary conditions, initially proposed in Guermond & Shen (2003). The current scheme incorporates the higher-order temporal accuracy and improved conditional stability for both velocity and pressure introduced in Wu *et al.* (2022*a*). Briefly, the momentum equation is discretised in time using a third-order backwards difference formula, BDF3, with the Euler force and the viscous terms treated implicitly and the nonlinear, Coriolis force and pressure terms evaluated explicitly via third-order extrapolation. An updated pressure is obtained by integrating against a gradient field, with the viscous term evaluated using the alternate formulation $\nabla^2 \boldsymbol{v} = -\nabla \times (\nabla \times \boldsymbol{v})$, which improves the accuracy of the computed pressure. The treatment of each stage leads to a decoupled system of Helmholtz-type equations with constant coefficients for the velocity and a Poisson equation with constant coefficients for the pressure. These are then spatially discretised using Legendre polynomials of degree ℓ in each of the three spatial directions for the velocity components

E:	10^{-6}	10^{-7}	10^{-8}	10^{-9}
ℓ:	150	200	350	550
n_t:	800	200	200	200

Table 1. Legendre polynomial degree, ℓ, and number of time steps per libration period, n_t, used for $\omega = 0.05$, $Ro \lesssim 10E$ and E as indicated.

and of degree $\ell - 2$ for the pressure. The nonlinear advection term is evaluated in physical space via projection from spectral space, and a zero-mean pressure condition is imposed by setting the constant basis pressure coefficient to 0. This results in a symmetric positive-definite banded system for the pressure, which is solved efficiently via diagonalisation.

In this study, we only present results for small $\omega = 0.05$ for which the foliation patterned topographic Rossby waves are prominent (Wu *et al.* 2022*b*). The spatial and temporal resolutions needed for numerical stability and accuracy are much larger for small ω than for $\omega \sim 1$ at the same E and Ro. Furthermore, these requirements increase for both decreasing E and increasing Ro. Table 1 lists the Legendre polynomial degree, ℓ, and number of time steps per libration period, n_t, needed in the simulations for $\omega = 0.05$ and $Ro \lesssim 10E$ for $E \in [10^{-9}, 10^{-6}]$.

The same numerical approach is used to solve the linear system (2.9), but without computing the nonlinear or time-dependent Coriolis terms. Not having to compute those terms represents significant computational savings.

4. The linear forced viscous response

For $E > 0$, solutions to the homogeneous linear system, (2.9) with $\boldsymbol{f} = \boldsymbol{0}$, viscously decay in time, $\boldsymbol{v}_0 \to \boldsymbol{0}$ (Greenspan 1968), whereas the librationally forced linear system, (2.9) with $\boldsymbol{f} \neq \boldsymbol{0}$, drives a synchronous temporally harmonic response. This response may include cavity modes as well as shear layers that for small E may be described as beams comprised of circularly polarised waves. The fate of the wavebeams in the container at $E = 0$ can be estimated via ray tracing using the linear inviscid unforced equations together with the reflection laws for circularly polarised waves. A problem with this approach, however, is that with this system being unforced, it says nothing about where the wavebeams originate from in the container, and being linear it says nothing about their initial energy. Considerations from small-E simulations of the librationally forced linear system help inform where the beams are emitted from. This is detailed in Wu *et al.* (2022*b*) and Welfert *et al.* (2023). Briefly, for the cube orientation under consideration and small ω, conic sheets of beams are emitted from polar vertices and planar sheets of beams are emitted from polar and tropical edges. These reflect on walls and eventually focus onto the equatorial edges and vertices. Figure 2 shows the traces of beams on the surface of the cube, in the equatorial plane $y = -z$ and in the meridional plane $x = 0$ that are respectively emitted from polar vertices, polar edges and tropical edges, as well as their superposition. The colours correspond to the enstrophy density level of the circularly polarised wave relative to its initial enstrophy density at emission, which is arbitrary. In the absence of viscous effects, $E = 0$, the enstrophy density of a beam remains the same between consecutive reflections, but changes upon reflections at the oblique walls due to focusing.

We now consider the librationally forced linear viscous system (2.9) at $\omega = 0.05$. Figure 3 shows snapshots of the enstrophy density $(\boldsymbol{\nabla} \times \boldsymbol{v}_0)^2$, scaled by E, and the
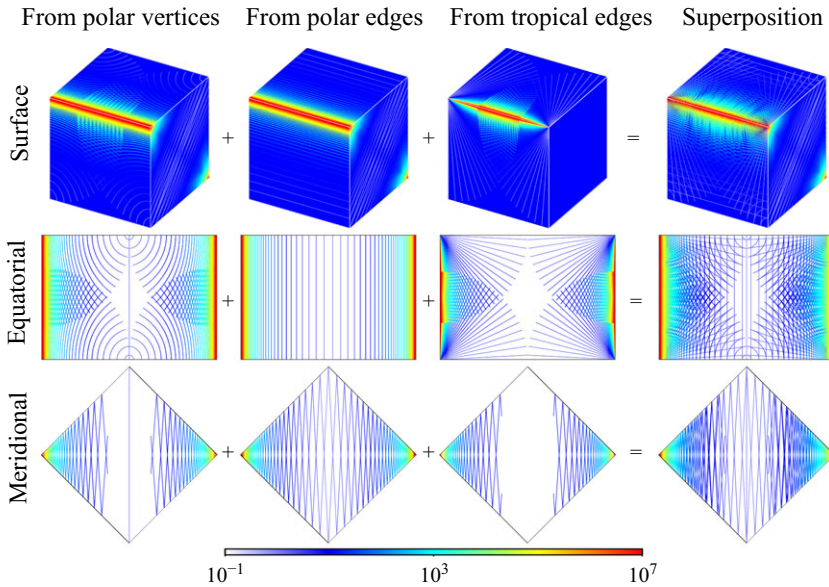
Figure 2. Traces of wavebeams, originating from various locations as indicated, on the cube surface and their intersections with the equatorial plane $y = -z$ and the meridional plane $x = 0$, obtained via ray tracing at $\omega = 0.05$. The colours correspond to the enstrophy density of a wavebeam relative to its initial enstrophy density at emission.

pressure q_0 on the cube surface and the equatorial and meridional planes for a range of E. The enstrophy density on the equatorial and meridional planes for $E = 10^{-9}$ has much in common with the linear inviscid ray tracing results shown in figure 2. The linear inviscid wavebeams correspond to the thin viscous vortex sheets that are emitted from the same edges and vertices. One difference is that for the linear inviscid ray tracing there is focusing along the entire equatorial edges, whereas the non-zero-E flows have intense peaks in $(\nabla \times \boldsymbol{v}_0)^2$ localised near the eastern equatorial vertices; $(\nabla \times \boldsymbol{v}_0)^2$ vanishes at the edges due to the no-slip boundary conditions. This difference is particularly evident on the surface plots. Moreover, the viscous shear layers do not focus all the way to the equatorial edges, particularly for increasing E: their focusing is viscously suppressed. Comparing the viscous results shown in the equatorial plane in figure 3 with the inviscid wavebeam analysis shown in figure 2, a loss of left–right and up–down symmetry is apparent. This is a consequence of the viscous term breaking the time-reversal symmetry of the inviscid problem (Wu *et al.* 2022*b*, equation (4.7)).

The distance d from the equatorial edge to where focusing appears to cease is indicated by a thin line in the plot of $(\nabla \times \boldsymbol{v}_0)^2$ in the equatorial plane (second row of figure 3). The distinct difference in flow dynamics either side of this line is better appreciated by viewing the animations in supplementary movie 1. This distance decreases with E, with $d = 500E^{1/2}$ ($d = 0.5$ for $E = 10^{-6}$). For decreasing E, the wavebeams associated with the thinner viscous shear layers have larger wavenumbers and their focusing reaches closer towards the equatorial edges. As they focus, the successive reflections on the oblique walls occur closer to each other, eventually resulting in viscous cross-annihilation (Stanaway, Shariff & Hussain 1988; Terrington, Hourigan & Thompson 2021) between incident and reflected vortex sheets.

In the regions near the equatorial edges devoid of the focusing shear layers, a very different flow behaviour is evident, corresponding to the foliated progressive waves
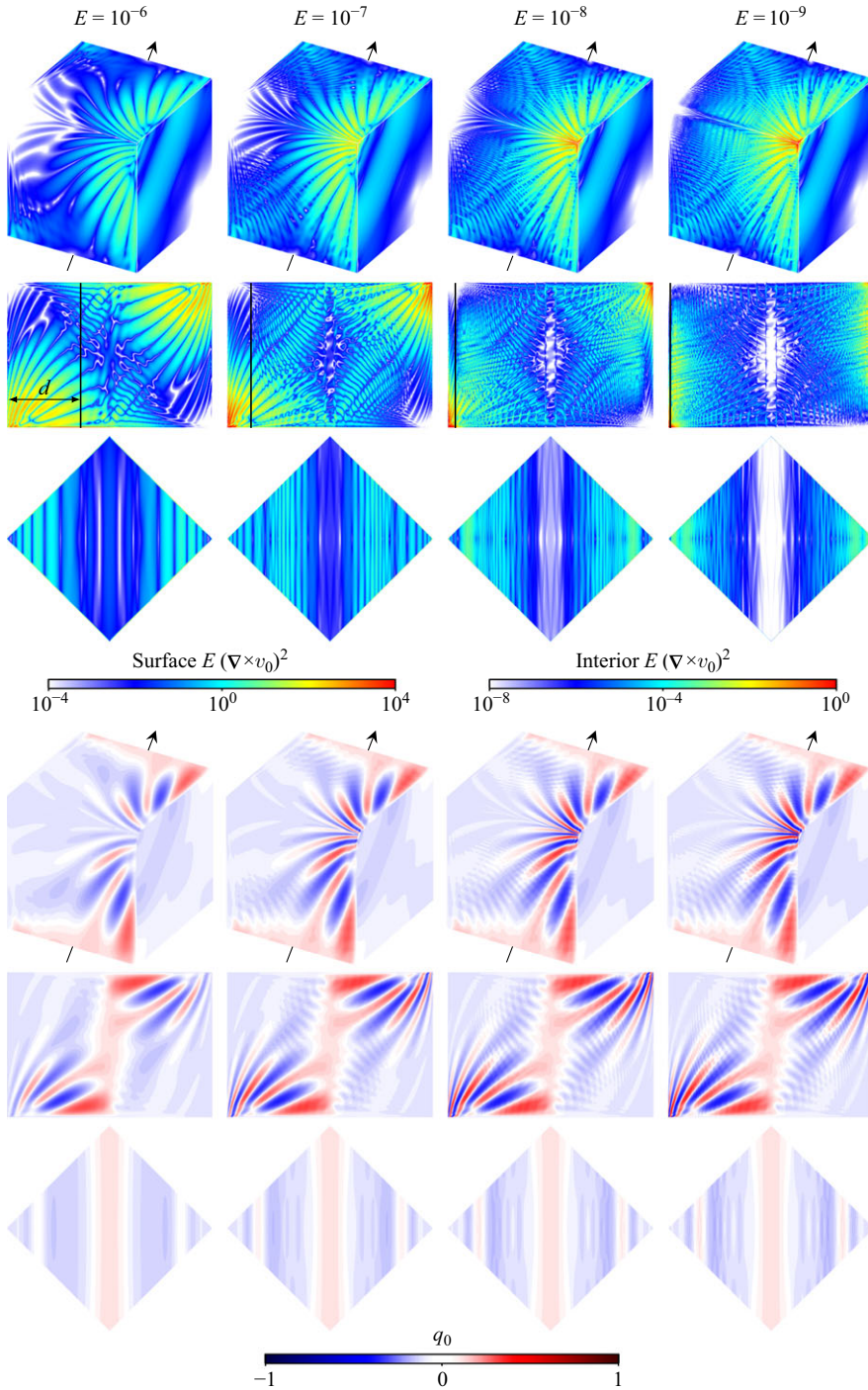
Figure 3. Snapshots of the linear response flows at $\omega = 0.05$ and E as indicated, showing $E(\nabla \times \boldsymbol{v}_0)^2$ and q_0 on the surface and in the equatorial and meridional planes. The cessation of focusing in a vicinity d of equatorial edges is indicated by a black line in the $(\nabla \times \boldsymbol{v}_0)^2$ equatorial planes. Supplementary movie $1(a, b)$ animates the surface and equatorial plane views for $E = 10^{-7}$ and 10^{-9} over one period.
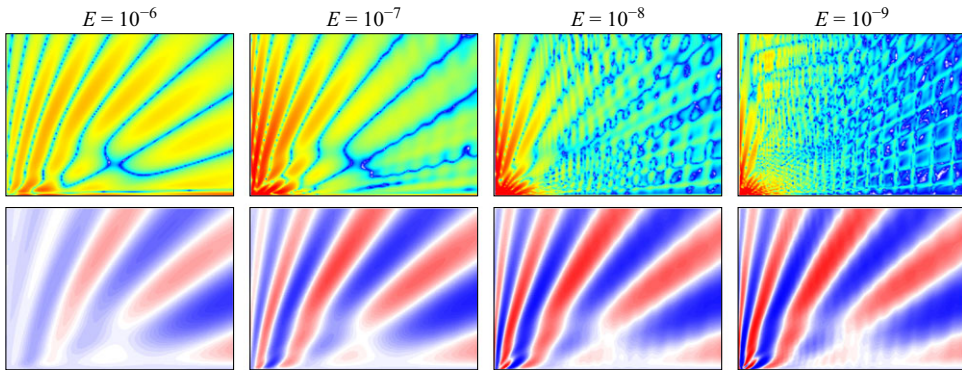
Figure 4. Zoom-ins ($\times 4$) around the equatorial vertex $(0.5, -0.5, 0.5)$ in the equatorial plane shown in figure 3 of $E(\nabla \times \mathbf{v}_0)^2$ (top) and q_0 (bottom).

mentioned in the Introduction. The focusing shear layers are related to the circularly polarised waves analysed in the linear inviscid ray tracing and hence their $(\nabla \times \mathbf{v}_0)^2$ traces remain fixed in space for all time. In contrast, the arms of the foliated waves emerge from the equatorial edges, with one end more-or-less fixed at the eastern equatorial vertices. They sweep out an arc in a retrograde fashion relative to the rotation axis and terminate at the walls $x = \pm 0.5$. This is illustrated in supplementary movie $1(a, b)$ where $(\nabla \times \mathbf{v}_0)^2$ for $E = 10^{-7}$ and 10^{-9} is animated over one libration period. The stationary sharp structures seen in the equatorial plane, particularly evident in the scaled enstrophy density at $E = 10^{-9}$ (top-right panel of figure 4), coincide very well with the linear inviscid ray tracings in figure 2. Superimposed with these are the retrograde foliated waves. For increasing E, the stationary peaks corresponding to the beams are absent in the regions near the equatorial edges and the foliated progressive waves remain the only contribution to the flow within the distance d of the equatorial edges.

To further explore these foliated waves, figure 3 also shows the pressure q_0 on the cube surface and in the equatorial and meridional planes. The pressure plots are particularly useful as the pressure contribution from the foliated waves completely dominates the contribution from the focusing shear layers. The meridional plane views at $x = 0$ as well as at the wall $x = 0.5$ show that the foliation pattern is quasi-independent of the axial direction. This is true for both $(\nabla \times \mathbf{v}_0)^2$ and q_0. Each alternating arm of the foliation has opposite signed q_0, and each half libration period an arm is mapped to the location of its neighbour in the retrograde direction, as shown in supplementary movie $1(a, b)$.

Figure 4 presents plots of $(\nabla \times \mathbf{v}_0)^2$ and q_0 in the equatorial plane shown in figure 3 zoomed in by a factor of 4 near the eastern equatorial vertex at $(x, y, z) = (0.5, -0.5, 0.5)$. For the largest $E = 10^{-6}$, the inertial wavebeams are absent and for diminishing E their presence becomes more evident in $(\nabla \times \mathbf{v}_0)^2$. The zoom-ins make it clearer that the spatial shape of $(\nabla \times \mathbf{v}_0)^2$ associated with the foliated waves remains invariant with E, while the wavebeams at smaller E focus closer to the equatorial edge and their superpositions with the foliated waves lead to an interference pattern. On the other hand, q_0 is almost entirely due to the foliated waves and it is even clearer that their structure is independent of E, at least for $E \leqslant 10^{-6}$. All these features point to the foliated progressive waves being forced topographic Rossby waves.

From figures 3 and 4, it is evident that $(\nabla \times \mathbf{v}_0)^2$ scales with E^{-1} almost everywhere throughout the cube, except in the vicinity of the eastern equatorial vertices where it grows much larger with decreasing E. In order to quantify this localised growth, we use an
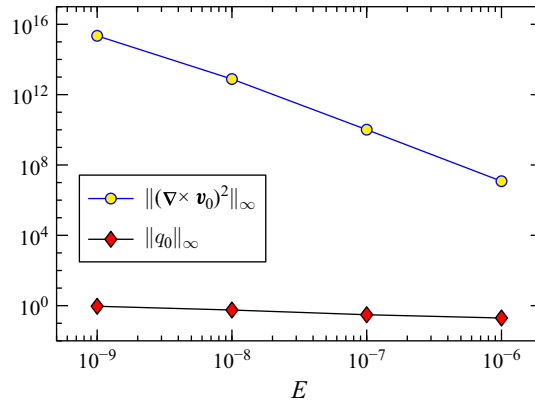
Figure 5. Variation with E of $\|(\boldsymbol{\nabla} \times \boldsymbol{v}_0)^2\|_\infty$ and $\|q_0\|_\infty$.

∞-norm, which is the maximum of a quantity Q throughout the cube over one libration period:

$$\|Q\|_\infty = \max\{|Q(\boldsymbol{x},\, t)| : \boldsymbol{x} \in [-0.5,\, 0.5]^3,\ t \in [t_a,\, t_a + \pi/\omega]\}. \tag{4.1}$$

The time t_a is a time after the flow has settled to a synchronous periodic state, typically corresponding to several dozen libration periods, with the number of periods increasing with decreasing E.

Figure 5 shows how the ∞-norms of $(\boldsymbol{\nabla} \times \boldsymbol{v}_0)^2$ and q_0 vary with E. The pressure scales weakly with E, with $\|q_0\|_\infty \propto E^{-1/6}$. In contrast, $\|(\boldsymbol{\nabla} \times \boldsymbol{v}_0)^2\|_\infty \propto E^{-8/3}$ grows much faster with decreasing E. The scaling of $(\boldsymbol{\nabla} \times \boldsymbol{v}_0)^2$ with E^{-1} almost everywhere throughout the cube, evident in figure 3, is to be expected from the development of thinner and more intense boundary layers and shear layers with decreasing E, whereas the much faster $E^{-8/3}$ scaling of $\|(\boldsymbol{\nabla} \times \boldsymbol{v}_0)^2\|_\infty$ is indicative of developing singularities near the two eastern equatorial vertices about which the foliation patterns pivot.

5. Nonlinear responses at small Ro

The development towards singularities in the enstrophy density strongly localised at the two eastern equatorial vertices with decreasing E raises the question of how the nonlinearities in the Navier–Stokes equations, so far neglected, affect their $E^{-8/3}$ scaling. Figure 6 shows snapshots of the enstrophy density $(\boldsymbol{\nabla} \times \boldsymbol{v})^2$ and pressure q on the cube surface and on the equatorial and meridional planes for the same E as in figure 3, but for $Ro = Ro_{max}(E)$, the largest values of Ro for each E for which we were able to compute a stable synchronous response flow. The spatial and temporal resolutions needed at $Ro = Ro_{max}(E)$ are listed in table 2. For the largest $E = 10^{-6}$, further increasing Ro leads to an instability introducing quasi-periodic behaviour. For smaller E, increasing Ro leads to temporal and spatial resolution requirements that made simulations of quasi-periodic responses prohibitive. This is due, as demonstrated below, to the developing singularities as E is decreased having large nonlinear effects even for very small non-zero Ro.

Comparing figures 3 and 6, as well as supplementary movies $1(a, b)$ and $1(c, d)$, there is virtually no difference between the enstrophy density and pressure at $Ro = 0$ and the larger Ro, except in the vicinity of the developing singularities near the two eastern equatorial vertices. To quantify these differences the synchronous flow $(\boldsymbol{v},\, q)$, computed from (2.7) at a given E and $0 < Ro \ll 1$, is decomposed as
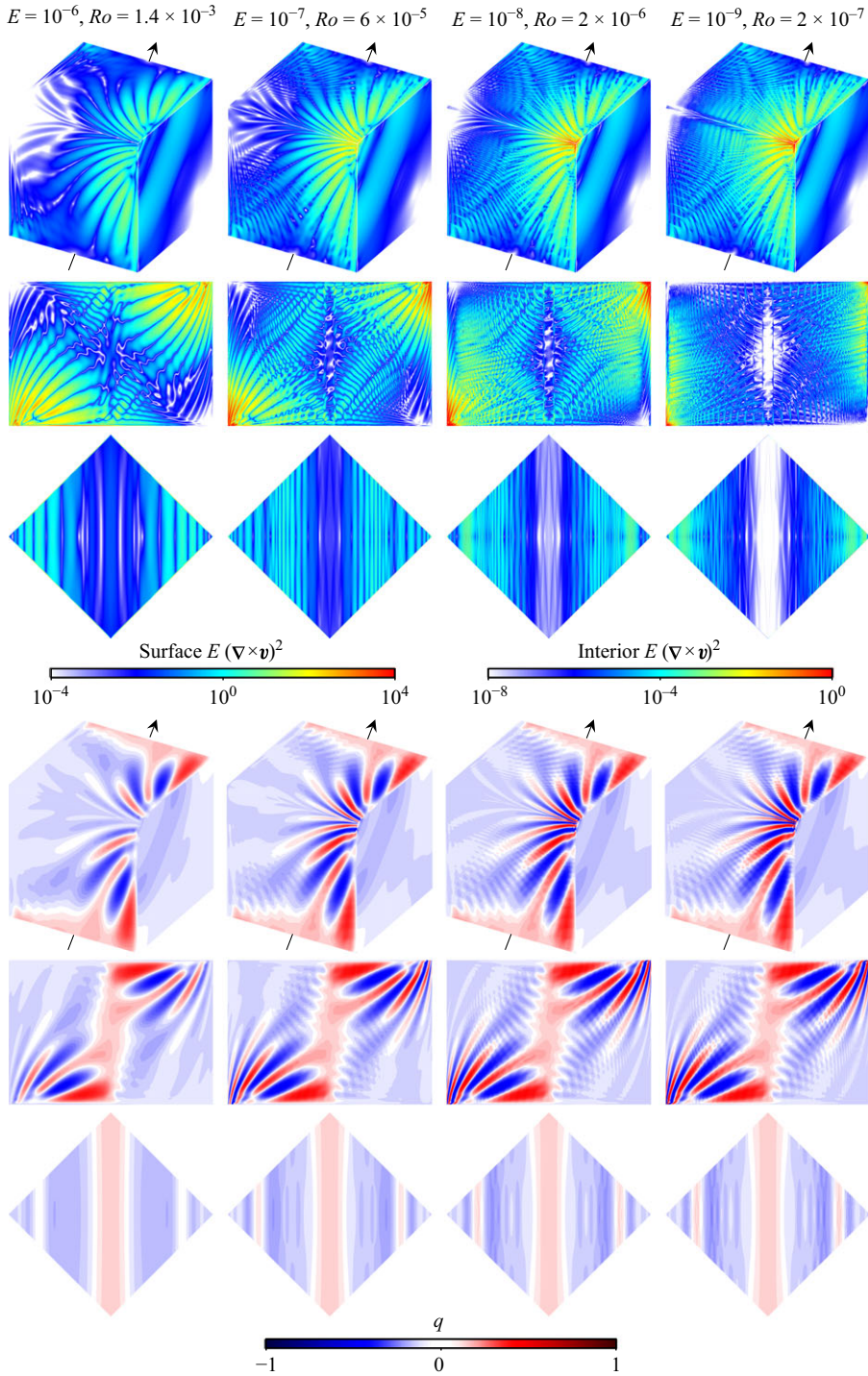
Figure 6. Snapshots of the symmetric synchronous response flows at $\omega = 0.05$ and E and Ro as indicated, showing $E(\nabla \times \boldsymbol{v})^2$ and q on the surface, equatorial and meridional planes. Supplementary movie 1(c, d) animates the surface and equatorial plane views for $E = 10^{-7}$ and 10^{-9} over one period.

E:	10^{-6}	10^{-7}	10^{-8}	10^{-9}
Ro:	1.4×10^{-3}	6×10^{-5}	2×10^{-6}	10^{-7}
ℓ:	200	350	400	600
n_t:	3200	2000	400	400

Table 2. Legendre polynomial degree, ℓ, and number of time steps per libration period, n_t, used for $\omega = 0.05$, $Ro = Ro_{max}(E)$ and E as indicated.
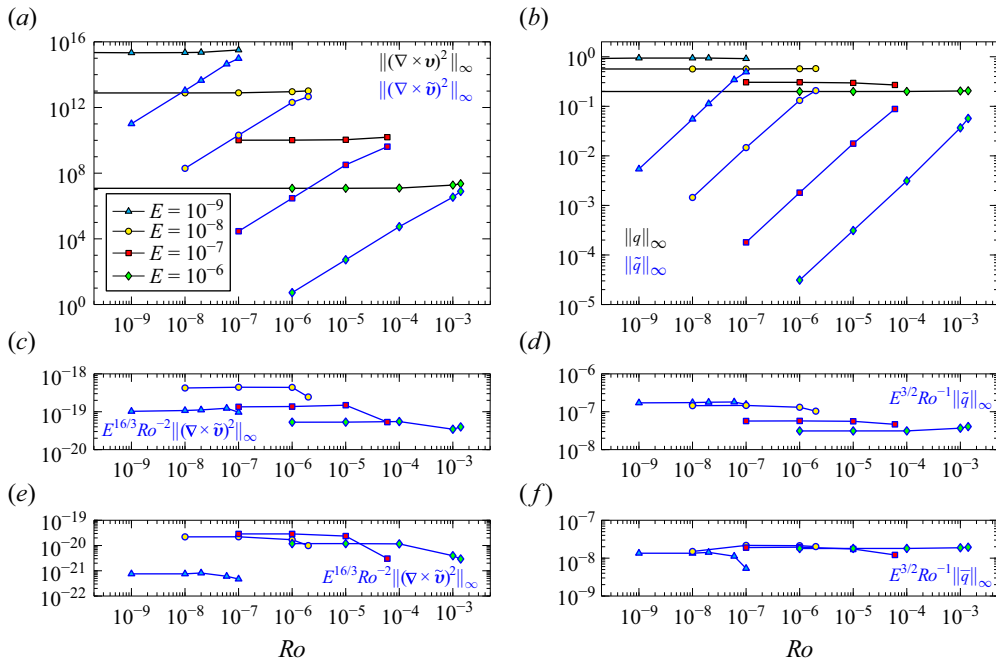

Figure 7. (a–f) Variation with Ro of the enstrophy and pressure ∞-norms of the various components in (5.1), as well as for the mean flow, for E as indicated.

$$\boldsymbol{v} = \boldsymbol{v}_0 + \widetilde{\boldsymbol{v}}, \quad q = q_0 + \widetilde{q}, \tag{5.1}$$

where $(\boldsymbol{v}_0, q_0)$ is the linear temporally harmonic flow (i.e. it has zero mean and no higher harmonics) computed from (2.9) at the same E and $(\widetilde{\boldsymbol{v}}, \widetilde{q})$ is time periodic containing all the nonlinear contributions from $(\boldsymbol{v}, q)$, i.e. the mean $(\overline{\boldsymbol{v}}, \overline{q})$ and all higher harmonics.

In order to minimise numerical errors in evaluating $(\widetilde{\boldsymbol{v}}, \widetilde{q})$, $(\boldsymbol{v}_0, q_0)$ is recomputed here using the same higher resolution used for $(\boldsymbol{v}, q)$, listed in table 2, compared with that from table 1, which was sufficient to obtain well-resolved $(\boldsymbol{v}_0, q_0)$.

The ∞-norms of the various components in (5.1) are shown in figure 7(a, b). The limits as $Ro \to 0$ of $\|(\nabla \times \boldsymbol{v})^2\|_\infty$ and $\|q\|_\infty$ are the values of $\|(\nabla \times \boldsymbol{v}_0)^2\|_\infty$ and $\|q\|_\infty$ shown in figure 5; $\|(\nabla \times \boldsymbol{v})^2\|_\infty$ and $\|q\|_\infty$ do not vary very much with Ro until $Ro \approx Ro_{max}$. On the other hand, $\|(\nabla \times \widetilde{\boldsymbol{v}})^2\|_\infty \propto Ro^2$ and $\|\widetilde{q}\|_\infty \propto Ro$, as expected from the quadratic nonlinearity in the Navier–Stokes equations. Figure 7(c, d) rescales $\|(\nabla \times \widetilde{\boldsymbol{v}})^2\|_\infty$ and $\|\widetilde{q}\|_\infty$ showing that the nonlinear contributions in the enstrophy density scale with $E^{-16/3}Ro^2$ and the nonlinear contributions in the pressure scale with $E^{-3/2}Ro$. These scalings are used in the colourmap scalings of $(\nabla \times \widetilde{\boldsymbol{v}})^2$ and $\widetilde{q}$ in figure 8, as well as the
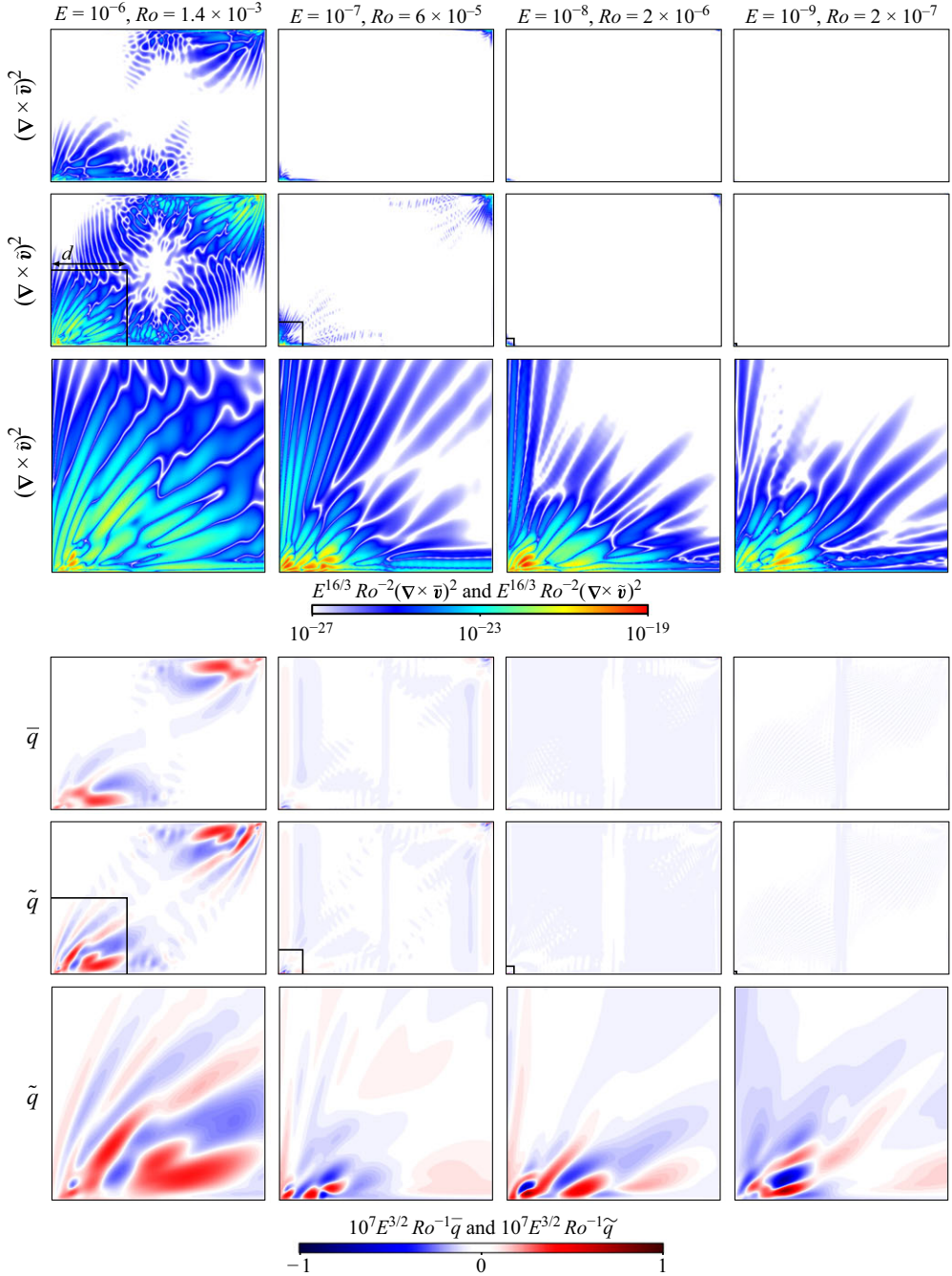
Figure 8. Snapshots of (top rows) the enstrophy density associated with the mean flow $\overline{\boldsymbol{v}}$, nonlinear contribution $\widetilde{\boldsymbol{v}}$, and (bottom rows) the mean pressure $\overline{q}$ and the pressure nonlinear contribution $\widetilde{q}$, in the equatorial plane for E and Ro as indicated. The $d \times d$ square corner insets, with d as in figure 3, delimit the zoom-in regions shown beneath each plot. Supplementary movie 2 animates the zoom-ins of $(\boldsymbol{\nabla} \times \widetilde{\boldsymbol{v}})^2$ and $\widetilde{q}$ over one libration period.

enstrophy density of the mean flow $(\nabla \times \overline{\boldsymbol{v}})^2$ and the mean pressure $\overline{q}$, which have the same scalings but slightly lower magnitudes, confirming that, as E decreases, the weakly nonlinear response flow is captured everywhere in the container by the linear component $(\boldsymbol{v}_0, q_0)$, except in regions around the two eastern equatorial vertices of size scaling with $d \sim E^{1/2}$. This is not surprising since Ro is quite small and the enstrophy density is dominated almost everywhere (i.e. everywhere except within a distance d of the equatorial edges) by the focusing shear layers which at these small values of E and Ro are essentially circularly polarised wavebeams, with $(\boldsymbol{v} \cdot \nabla)\boldsymbol{v} = 0$ for individual beams.

Zoom-ins of the enstrophy densities associated with the nonlinear contributions $(\widetilde{\boldsymbol{v}}, \widetilde{q})$ in a $d \times d$ square region of the eastern equatorial vertices, indicated in the plots of $(\nabla \times \widetilde{\boldsymbol{v}})^2$ and $\widetilde{q}$ in figure 8, are also shown in that figure and animated over one libration period in supplementary movie 2. In order to avoid pixelation effects resulting from repeated zoom-ins, the spectral solution was projected onto finer physical grids for each panel. The similar structure of the last three panels for each quantity confirms both the spatial extent, $\mathcal{O}(E^{1/2})$, and magnitudes, $\mathcal{O}(E^{-16/3}Ro^2)$, for the enstrophy density and $\mathcal{O}(E^{-3/2}Ro)$ for the pressure, corresponding to the nonlinear contributions.

The above (Ro, E)-dependent scalings raise the question of how small Ro should be compared with E in order for the linear approximation $(\boldsymbol{v}, q) \simeq (\boldsymbol{v}_0, q_0)$ to be globally valid. From the scalings inferred from figures 5 and 7, we have $\|(\nabla \times \boldsymbol{v}_0)^2\|_\infty \sim E^{-8/3}$ and $\|(\nabla \times \widetilde{\boldsymbol{v}})^2\|_\infty \sim E^{-16/3}Ro^2$, so that $\|(\nabla \times \widetilde{\boldsymbol{v}})^2\|_\infty / \|(\nabla \times \boldsymbol{v}_0)^2\|_\infty \sim E^{-8/3}Ro^2$. For this to be smaller than some acceptable tolerance $\mathcal{T}^2$, we must have

$$Ro < E^{4/3}\mathcal{T}. \tag{5.2}$$

The scalings from figures 5 and 7 also show $\|q_0\|_\infty \sim E^{-1/6}$ and $\|\widetilde{q}\|_\infty \sim E^{-3/2}Ro$, so that $\|\widetilde{q}\|_\infty / \|q_0\|_\infty \sim E^{-4/3}Ro$, which is smaller than the tolerance $\mathcal{T}$ under the same condition (5.2). So, for the small-forcing-amplitude flows to be globally well approximated by the linear flows, keeping Ro approximately smaller than $E^{4/3}$ is necessary.

6. Conclusion

A detailed investigation of low-frequency librational forcing of the flow in a rapidly rotating cube oriented with the rotation axis bisecting two diagonally opposite edges has revealed the presence of topographic Rossby waves. This orientation of the cube has no closed geostrophic contours, a condition conducive for Rossby waves. Furthermore, the fluid depth (distance parallel to the rotation axis between bounding walls) vanishes at the equatorial edges (edges furthest away from the rotation axis). It is from these edges that the libration-driven Rossby waves emerge into the interior, where they propagate in a retrograde fashion. Their overall structure consists of a foliation pattern, with one foliation arm being emitted every half libration period, with alternate arms having opposite-signed pressure.

The shape of the Rossby waves is independent of both the Ekman number E and the Rossby number Ro. The enstrophy density of the Rossby waves for small libration amplitudes $(0 \leqslant Ro < E^{1/2})$ scales with E^{-1} almost everywhere throughout the cube, except in a small region about the eastern equatorial vertices about which the Rossby waves quasi-rotate. The length scale of this region scales with $E^{1/2}$, which is typical of viscous boundary-layer length scales. It is inside this region where the enstrophy density associated with the nonlinear aspects of the flow is highly concentrated and scales in magnitude as $E^{-16/3}Ro^2$, in large part due to vortex stretching. The librational forcing also drives thin shear layers from the other edges and vertices into the interior. These shear layers correspond to circularly polarised wavebeams which have been extensively

studied via ray tracing in the linear inviscid setting, with a prediction of focusing onto the equatorial edges following reflections on the walls oblique to the rotation axis. However, for finite E, we find that the focusing is arrested via viscous annihilation at a distance from the equatorial edges that also scales as $E^{1/2}$.

Topographic Rossby waves are typically studied in systems with small variations in the fluid depth, e.g. a sliced cylinder with large depth and small inclination angle (Pedlosky & Greenspan 1967; Beardsley & Robbins 1975; Becker & Page 1990). This allows for a quasi-geostrophic description, whereby the governing equations are reduced to a forced axially averaged system. While this approach facilitates the study of the topographic Rossby waves, it filters out the circularly polarised inertial waves. Allowing the depth to have large variations leads to strongly nonlinear behaviour (Griffiths & Kiss 1999; Kiss 2003). If the depth vanishes at some point in the geometry, the quasi-geostrophic approximations are no longer valid. This is the case for our geometry with the depth vanishing at the equatorial edges, necessitating the use of the fully three-dimensional Navier–Stokes equations.

References

BEARDSLEY, R.C. 1975 The sliced-cylinder laboratory model of the wind-driven ocean circulation. Part 2. Oscillatory forcing and Rossby wave resonance. *J. Fluid Mech.* **69** (1), 41–64.

BEARDSLEY, R.C. & ROBBINS, K. 1975 The sliced-cylinder laboratory model of the wind-driven ocean circulation. Part 1. Steady forcing and topographic Rossby wave instability. *J. Fluid Mech.* **69** (1), 27–40.

BECKER, A. & PAGE, M.A. 1990 Flow separation and unsteadiness in a rotating sliced cylinder. *Geophys. Astrophys. Fluid Dyn.* **55** (2), 89–115.

BOURY, S., SIBGATULLIN, I., ERMANYUK, E., SHMAKOVA, N., ODIER, P., JOUBAUD, S., MAAS, L.R.M. & DAUXOIS, T. 2021 Vortex cluster arising from an axisymmetric inertial wave attractor. *J. Fluid Mech.* **926**, A12.

GREENSPAN, H.P. 1968 *The Theory of Rotating Fluids*. Cambridge University Press.

GREENSPAN, H.P. 1969 On inviscid theory of rotating fluids. *Stud. Appl. Maths* **48** (1), 19–28.

GRIFFITHS, R.W. & KISS, A.E. 1999 Flow regimes in a wide sliced-cylinder model of homogeneous beta-plane circulation. *J. Fluid Mech.* **399**, 205–236.

GUERMOND, J.-L. & SHEN, J. 2003 A new class of truly consistent splitting schemes for incompressible flows. *J. Comput. Phys.* **192** (1), 162–176.

LORD, K. 1880 Vibrations of a columnar vortex. *Phil. Mag.* **10**, 155–168.

KISS, A.E. 2003 A modified quasigeostrophic formulation for weakly nonlinear barotropic flow with large-amplitude depth variations. *Ocean Model.* **5** (2), 171–191.

LE DIZÈS, S. 2020 Reflection of oscillating internal shear layers: nonlinear corrections. *J. Fluid Mech.* **899**, A21.

LE DIZÈS, S. 2024 Critical slope singularities in rotating and stratified fluids. *Phys. Rev. Fluids* **9** (3), 034803.

MAAS, L.R.M. 2001 Wave focusing and ensuing mean flow due to symmetry breaking in rotating fluids. *J. Fluid Mech.* **437**, 13–28.

MANDERS, A.M.M. & MAAS, L.R.M. 2003 Observations of inertial waves in a rectangular basin with one sloping boundary. *J. Fluid Mech.* **493**, 59–88.

PEDLOSKY, J. & GREENSPAN, H.P. 1967 A simple laboratory model for the oceanic circulation. *J. Fluid Mech.* **27** (2), 291–304.

PHILLIPS, O.M. 1963 Energy transfer in rotating fluids by reflection of inertial waves. *Phys. Fluids* **6** (4), 513–520.

RIEUTORD, M., GEORGEOT, B. & VALDETTARO, L. 2000 Wave attractors in rotating fluids: a paradigm for ill-posed Cauchy problems. *Phys. Rev. Lett.* **85** (20), 4277–4280.

RIEUTORD, M., GEORGEOT, B. & VALDETTARO, L. 2001 Inertial waves in a rotating spherical shell: attractors and asymptotic spectrum. *J. Fluid Mech.* **435**, 103–144.

SHIRYAEVA, M., SUBBOTINA, M. & SUBBOTIN, S. 2024 Linear and non-linear dynamics of inertial waves in a rotating cylinder with antiparallel inclined ends. *Fluid Dyn. Mater. Process.* **20** (4), 787–802.

STANAWAY, S., SHARIFF, K. & HUSSAIN, F. 1988 Head-on collision of viscous vortex rings. Tech. Rep. CTR-S88, Proc. Summer Program, Center for Turbulence Research.

SUBBOTIN, S., SHMAKOVA, N., KOZLOV, V. & ERMANYUK, E. 2023 Nonlinear regimes of inertial wave attractors generated by a precessing lid: zonal flows and Rossby waves. *Phys. Fluids* **35** (7), 074110.

TERRINGTON, S.J., HOURIGAN, K. & THOMPSON, M.C. 2021 The generation and diffusion of vorticity in three-dimensional flows: Lyman's flux. *J. Fluid Mech.* **915**, A106.

WELFERT, B.D., LOPEZ, J.M. & WU, K. 2023 Inertial wave attractors in rapidly rotating tilted cuboids. *Proc. R. Soc. Lond. A* **479** (2272), 20220876.

WOOD, W.W. 1966 An oscillatory disturbance of rigidly rotating fluid. *Proc. R. Soc. Lond. A* **293** (1433), 181–212.

WU, K., HUANG, F.K. & SHEN, J. 2022*a* A new class of higher-order decoupled schemes for the incompressible Navier–Stokes equations and applications to rotating dynamics. *J. Comput. Phys.* **458**, 111097.

WU, K., WELFERT, B.D. & LOPEZ, J.M. 2022*b* Reflections and focusing of inertial waves in a tilted librating cube. *J. Fluid Mech.* **947**, A10.

WU, K., WELFERT, B.D. & LOPEZ, J.M. 2023 Inertial wave attractors in librating cuboids. *J. Fluid Mech.* **973**, A20.